Tunable Near-Field Radiative Effect in a T_d–WTe_2 Single Layer

Cheng-Long Zhou,[1,2] Zahra Torbatian,[3] Xiao-Hu Wu,[4] Yong Zhang,[1,2] Hong-Liang Yi,[1,2,*] and Dino Novko[5,6,†]

[1] *School of Energy Science and Engineering, Harbin Institute of Technology, Harbin 150001, People's Republic of China*

[2] *Key Laboratory of Aerospace Thermophysics, Ministry of Industry and Information Technology, Harbin 150001, People's Republic of China*

[3] *School of Nano Science, Institute for Research in Fundamental Sciences (IPM), Tehran 19395-5531, Iran*

[4] *Shandong Institute of Advanced Technology, Jinan 250100, Shandong, People's Republic of China*

[5] *Institute of Physics, Zagreb 10000, Croatia*

[6] *Donostia International Physics Center (DIPC), Donostia, San Sebastián 20018, Spain*

(Received 16 October 2021; revised 19 December 2021; accepted 4 January 2022; published 31 January 2022)

In contrast to artificial metamaterials, natural two-dimensional (2D) hyperbolic materials are able to support higher electromagnetic confinement and stronger photonic density of states. This means natural 2D hyperbolic materials have fascinating potential for applications in thermal photonics. In this work, we investigate mechanisms of near-field thermal radiation (NFTR) in a T_d–WTe_2 single layer at the nanoscale using the fluctuation-dissipation theorem and density-functional theory. The results show that NFTR of T_d–WTe_2 can be 3 orders of magnitude larger than the blackbody limit. By using the photonic tunneling coefficient and the plasmon dispersion, we present a comprehensive study of plasmonic properties of T_d–WTe_2. Moreover, our first-principles calculations predict that application of a certain amount of mechanical stress can trigger topological transition between the elliptic and the hyperbolic surface states by regulating the Fermi surface and interband excitation threshold. Lastly, we systematically exhibit the evolution of surface plasmon polaritons in T_d–WTe_2 under mechanical stress and analyze the performance of using mechanical stress to modulate the corresponding NFTR. Our work explores the great potential of tunable radiative heat flux in T_d–WTe_2, which is explained here through the peculiar nature of hyperbolic surface plasmons.

DOI: 10.1103/PhysRevApplied.17.014044

I. INTRODUCTION

Near-field thermal radiation (NFTR) is a high-efficiency energy transport at the nanoscale, which can be far ahead of the blackbody limit by several orders of magnitude due to the contribution from tunneling of evanescent modes [1–4]. This huge radiative heat flux at the nanoscale not only attracts particular scientific interest triggered by experimental advances [5–10], but also enables a series of potential applications, like thermal lithography [11], photon transformer [12], thermal router [13,14], thermal logical circuitry [15–20], and high-efficiency energy-conversion technology [21–26]. Since the huge heat flux is extremely useful in these applications, over the past decade, continuous efforts have been devoted to maximize NFTR by exploring innovative structures or materials. Typically, one valuable strategy relies on hyperbolic materials that support broadband polaritons with high wave vector, such as wire-hole media [27–30], layered metal-dielectric structure [31–33], and nanogratings [34–36]. Approaches based on this idea have produced remarkable results in the enhancement of NFTR. For instance, Biehs *et al*. found that the broadband spectra of hyperbolic modes supported by periodic nanowires enable such systems to get heat fluxes larger than the ones due to narrowband-coupled surface-polariton modes [28]; Liu *et al*. reported that patterning silicon thin films as nanograting with hyperbolic modes can substantially enhance the heat fluxes by more than one order of magnitude [35]. However, in these artificial metamaterials, the constrained hyperbolic modes stand as a major obstacle to further enhance the NFTR, because its wave vector must be smaller than π/P (P is a period of structure) [37]. Besides, complex nanoprocessing technology is also a non-negligible roadblock.

Alternatively, recent studies have predicted that natural two-dimensional (2D) materials, supporting anisotropic geometry and peculiar interplay between intraband and

*yihongliang@hit.edu.cn
†dino.novko@gmail.com

interband electronic transitions, can also sustain hyperbolic surface plasmon polaritons (HSPPs) [38,39]. In contrast to artificial metamaterials, natural hyperbolic surfaces enable unprecedented potential in planar photonics, sparking the development of schemes to modulate and harvest the electromagnetic energy flow [40,41]. However, natural 2D hyperbolic materials have remained elusive. Although some anisotropic 2D materials are predicted to potentially realize 2D hyperbolic plasmons, e.g., black phosphorous [42] and carbon phosphide [43], the experimental achievement of 2D hyperbolic materials has not been reported. In 2020, a natural 2D hyperbolic material was disclosed by Wang *et al.*, who demonstrated the existence of natural hyperbolic plasmonic through exfoliated T_d–WTe_2 [44]. The reported hyperbolic plasmons pave the way for the realization of flatland photonics at THz and mid-IR frequencies without artificial structuring [45]. In comparison with hyperbolic phonon polaritons of MoO_3 and *h*-BN, the reduction of dielectric screening in 2D crystals leads to inherently stronger coupling of its plasmon polaritons and light [46,47]. Moreover, the hyperbolic properties of this 2D material have high degrees of freedom and can be tuned dynamically through modifications in the band structure induced by external modulation. All these render WTe_2 an exciting platform with 2D hyperbolic plasmons, which opens up exotic avenues for the manipulation of plasmon propagation, light-matter interaction, and light emission. The fundamental studies for this 2D hyperbolic material, however, are still very scarce, especially in the field of thermal radiation, which hinders its further exploration and practical application.

In this paper, we investigate the mechanisms of radiative heat transport in T_d–WTe_2 using the fluctuation-dissipation theorem and density-functional theory. The elliptical and hyperbolic plasmonic properties of this 2D semimetal are exhibited by using a photonic tunneling coefficient and plasmon dispersions, and the role of different SPPs on NFTR is revealed. Moreover, we perform the influence of mechanical stress on hyperbolic properties in T_d–WTe_2 and then investigate how to efficiently tune the NFTR of T_d–WTe_2 by applying mechanical stress, hoping to offer guidance to manipulate the NFTR. Finally, the results of this research are summarized in the conclusion.

II. MODEL AND METHOD

We consider the near-field thermal radiation model consisting of two parallel monolayer T_d–WTe_2 sheets with a vacuum gap d (see Fig. 1). Here, we define the monolayer T_d–WTe_2 sheet as a suspended system to hedge the interference or hybridization effect of the substrate. Suspended systems are widely used for studying the mechanisms of radiative heat transport in alternative materials and structures, including but not limited to 2D sheets [48–53], 2D gratings [54], and 2D disks [55]. In addition, the mechanism discovered in the suspended system is extremely useful, providing a basis for the realistic coated system. The temperatures of the top and bottom T_d–WTe_2 sheets are T and $T+\Delta T$, respectively, in which T is equal to 300 K (room temperature). In this work, we focus on the analysis of the radiative heat conductance per unit of area, h (in units of W m^{-2} K^{-1}), which is called the heat-transfer coefficient (HTC). This coefficient is given by [56]

$$h(T,d)=\int_0^\infty h(\omega)d\omega=\frac{1}{8\pi^3}\int_0^\infty\frac{\partial\Theta(\omega,T)}{\partial T}d\omega\int_{-\infty}^{\infty}\int_{-\infty}^{\infty}\xi(\omega,k_x,k_y)dk_xdk_y, \tag{1}$$

where $\Theta(\omega,T)=\hbar\omega/[exp(\hbar\omega/k_BT)-1]$ is the mean photon energy of a Planck oscillator at angular frequency ω and temperature T. k_x and k_y are the surface wave vectors along the x and y axis, respectively. When the surface parallel wave vector $k=\sqrt{k_x^2+k_y^2}$ is greater than the wave vector in vacuum $k_0=\omega/c_0$, the electromagnetic wave excited by thermal energy is the evanescent wave [57]. Otherwise, it is the propagating wave. $\xi(\omega,k_x,k_y)$ is the photonic tunnelling coefficient (PTC) of thermal photons, and is expressed as [58]

$$\xi(\omega,k_x,k_y)=\begin{cases}\mathrm{Tr}[(\mathbf{I}-\mathbf{R}_2^*\mathbf{R}_2-\mathbf{T}_2^*\mathbf{T}_2)\mathbf{D}\,(\mathbf{I}-\mathbf{R}_1\mathbf{R}_1^*-\mathbf{T}_1^*\mathbf{T}_1)\mathbf{D}^*], & k<k_0\\ \mathrm{Tr}[(\mathbf{R}_2^*-\mathbf{R}_2)\mathbf{D}(\mathbf{R}_1-\mathbf{R}_1^*)\mathbf{D}^*]e^{-2|k_{z0}|d}, & k>k_0\end{cases}. \tag{2}$$

The identity matrix is denoted as **I**. Here, subscripts 1 and 2 represent the emitter (bottom sheet) and receiver (top sheet), respectively. $k_{z0}=\sqrt{k_0^2-k^2}$ is the tangential wave vector along z direction in vacuum. The reflection coefficient matrix $\mathbf{R}_n$ and the transmission coefficient matrix $\mathbf{T}_n$ at the interface between air and T_d–WTe_2 with $n=1$, 2 have the following forms [59]:

$$\mathbf{R}_n=\begin{bmatrix}r_n^{ss} & r_n^{sp}\\ r_n^{ps} & r_n^{pp}\end{bmatrix};\quad \mathbf{T}_n=\begin{bmatrix}t_n^{ss} & t_n^{sp}\\ t_n^{ps} & t_n^{pp}\end{bmatrix} \tag{3}$$

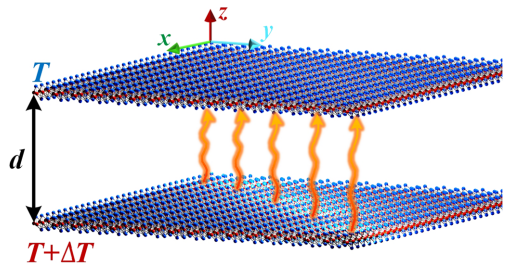

FIG. 1. Schematic of near-field thermal radiation between two monolayer T_d–WTe_2 sheets. Two parallel sheets are separated by a vacuum gap d. The temperature of the bottom T_d–WTe_2 sheet is higher than that of the top one.

and are provided in the Supplemental Material [60]. The 2×2 matrix $\mathbf{D}$ is defined as $\mathbf{D}=(\mathbf{I}-\mathbf{R}_1\mathbf{R}_2e^{2ik_{z0}d})^{-1}$, which describes the usual Fabry-Perot-like denominator, resulting from multiple scattering between emitter and receiver.

To provide some insight into the crystalline structure of T_d–WTe_2, we present in Figs. 2(a)–2(c) the top, front, and side views of the monolayer T_d–WTe_2, respectively. Compared to most transition metal dichalcogenides with prismatic or monoclinic trigonal structures, in this monolayer WTe_2, the tellurium (Te) octahedron is slightly distorted and the tungsten (W) atoms displace from their ideal octahedral sites, forming zigzag metal-metal chains [Fig. 2(b)]. This orthorhombic phase, T_d, is the most stable structure for WTe_2 compared to other polymorphs [69,70]. Therefore, in this work, we focus only on the T_d phase. Here, we define the direction of the W chain as the x axis and its vertical direction as the y axis. The electronic band structure for monolayer T_d–WTe_2 along the high-symmetry points S–Y–Γ–X–S in the orthorhombic unit cell is sketched in Fig. 2(d), and the calculating procedure is given in Ref. [71]. The electronic band structure of T_d–WTe_2 [Fig. 2(d)] exhibits distinct difference between Γ–X and Γ–Y, which is in good agreement with previous reports [41]. This larger anisotropy leads to significant difference in electron motion along the two main axes, implying intrinsic in-plane anisotropy for the optical properties of T_d–WTe_2. The optical properties of monolayer T_d–WTe_2 can be obtained by using the current-current response tensor calculated within fluctuation dissipation theorem [72,73]. To ensure that both lattice constants and atomic positions are sufficiently relaxed, the atomic positions are relaxed until the Hellmann-Feynman forces are less than 10^{-4} eV/Å and convergence criterion for the energy is less than 10^{-5} eV. The lattice constants are $a=3.671$ Å, and $b=6.642$ Å. The kinetic cut-off energy is 50 Ry and the Brillouin-zone integrations for the ground state are performed using a-centered grid of $24\times 24\times 1$ by using the QuantumEspresso code [74]. The current-current response tensor can be expressed as

$$\Pi^0_\mu(\mathbf{q},\omega)=\frac{2}{V}\sum_{\mathbf{k},n,m}\frac{\hbar\omega}{E_n(\mathbf{k})-E_m(\mathbf{k}+\mathbf{q})}\times\left|J^\mu_{kn,k+qm}\right|^2\frac{f_n(\mathbf{k})-f_m(\mathbf{k}+\mathbf{q})}{\hbar\omega+i\eta+E_n(\mathbf{k})-E_m(\mathbf{k}+\mathbf{q})}. \quad (4)$$

Here, V, $J^\mu_{kn,k+qm}$, and $E_n(\mathbf{k})$ represent the normalized volume, the current vertices, and the Kohn-Sham energies [72], respectively. $f_n(\mathbf{k})$ is the Fermi-Dirac distribution for temperature T. The index n or m sums over 30 electronic bands, and the summation of the momentum wave vector $\mathbf{k}$ is performed on a $120\times 60\times 1$ grid. It should be noted that the polarization directions μ are xx and yy. Further, the optical conductivity can be calculated as $\sigma_\mu=-i\lim_{\mathbf{q}\to 0}\Pi^0_\mu(\mathbf{q},\omega)/\omega$, in which $\mathbf{q}$ is a vector parallel to the surface [41]. The anisotropic optical conductivities for the orthogonal directions are plotted in Fig. 2(e). The signs of the imaginary part of the optical conductivity along two principal axes determine the topology of the plasmonic surface. At low frequency, both conductivity components have a positive imaginary part, producing an elliptical plasmonic response. When the frequency increases above the transition point of 0.19 eV/$\hbar$, $\mathrm{Im}(\sigma_{yy})$ turns to be negative and the surface behaves as a dielectric along this direction, thus opening the hyperbolic window of this material.

III. NEAR-FIELD ENHANCEMENT EFFECT OF THIS 2D MATERIAL

To get a more visual observation of these topology of the plasmonic surface, we now turn to discussion of photonic tunneling coefficient and dispersion relation. In Fig. 3, we plot $\xi(\omega, k_x, k_y)$ with $d=10$ nm at four frequencies in k_x–k_y plane, respectively. The wave vector is normalized by the wave vector in vacuum. These contours clearly illustrate the topological structure of the surface state in T_d–WTe_2 at different frequencies. First, the PTC contour for the excitation frequency of 0.05 eV/$\hbar$ is shown in Fig. 3(a). We can see an elliptical bright region in the contour, which indicates good agreement with the prediction of optical conductivity in Fig. 2(c). In this case, the degree of anisotropy ($\mathrm{Im}[\sigma_{xx}]/\mathrm{Im}[\sigma_{yy}]$) is 8.62, which results in a significant canalization along the x axis (W chain) as shown in Fig. 3(a). Meanwhile, in Fig. 3(a), the PTC, especially along the x axis, splits into two resonance branches, namely, antisymmetric modes at small wave vector and symmetric modes at large wave vector. The phenomenon is strongly related to the hybridization effect between evanescent fields aroused by the lower and upper vacuum-surface interfaces [75]. To verify that elliptical surface plasmon polaritons (ESPPs) are indeed responsible for NFTR at this frequency, we also draw the in-plane dispersion contour (blue line) in Fig. 3(a), which is derived by the in-plane dispersion formulation for 2D material in Ref. [50]. It can

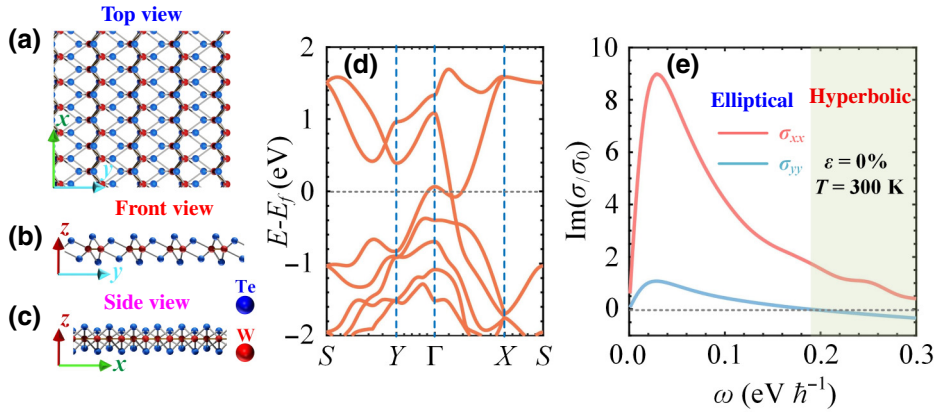

FIG. 2. (a) Top, (b) front, and (c) side views of monolayer T_d–WTe_2. Te atom and W atom are denoted by the blue sphere and the red sphere, respectively. The direction of the W chain is indicated as the x axis and its vertical direction is denoted as the y axis. (d) Electronic band structures for the monolayer T_d–WTe_2 along the high-symmetry points S–Y–Γ–X–S in the orthorhombic unit cell. (e) The imaginary parts of the optical conductivity along the x axis (red) and the y axis (blue). The hyperbolic regime is represented by a shaded area, where $\mathrm{Im}\,(\sigma_{xx}) \times \mathrm{Im}\,(\sigma_{yy}) < 0$.

be seen in Fig. 3(a) that the result obtained from the in-plane dispersion matches very well with the bright elliptical branches. Moreover, we notice that as the frequency increases to 0.1 eV/$\hbar$, the PTC not only extends to the high wave-vector region along y axis, but also exhibits stronger in-plane anisotropy with $\mathrm{Im}[\sigma_{xx}]/\mathrm{Im}[\sigma_{yy}]$ equal to 9.69. In this scenario, the PTC along the y axis extends to a high wave-vector region in comparison with the ones along the x axis, as depicted in Fig. 3(b). A similar trend is observed in plasmon dispersion in Fig. 3(b). For the frequency of 0.12 eV/$\hbar$, Fig. 3(c) shows that the PTC along the y axis occupies a broad wave-vector region but the corresponding values give rise to a significant recession. In contrast, the PTC along the x axis retains a higher value, which means that the coupling of SPPs along the x axis dominates the NFTR at a higher frequency. When the frequency increases to the hyperbolic region ($\omega = 0.19$ eV/$\hbar$), Fig. 3(d) shows that the bright branches evolve from an ellipse to a hyperbola, and this topological transition is also demonstrated in the in-plane plasmon dispersion.

When the frequency increases above the transition point, the PTC resonance branches and plasmon dispersion along the y axis would disappear, helping us to clearly identify the topological nature of the material, but this phenomenon does not appear on the x axis. Thus, to clearly identify the topological nature (hyperbolic and elliptic) of the material, we also plot the PTC and plasmon dispersion along the y axis ($k_x = 0$) in the (ω, k_y) plane [Fig. 3(e)]. It can be seen in Fig. 3(e) that, for the low-frequency region, there are bright resonant branches along the dispersion. As the frequency increases, the wave vector of the supported SPPs rapidly increases. However, it can be seen that the bright branches do not extend significantly into the larger wave-vector region (>300 k_0) with the dispersion curve in Fig. 3(e). This is because the attenuation length of the surface mode in the high wave-vector region decreases sharply. At the higher wave-vector region, the evanescent wave is easily filtered by the vacuum gap [76], which no longer stimulates obvious SPP coupling effect between two monolayer T_d–WTe_2 sheets. Besides, as the frequency is very close to the transition frequency, since the $\mathrm{Im}[\sigma_{yy}] \approx 0$, the dispersion along the y axis in (ω, k_y) plane would extend to the infinite wave-vector region and tend to be parallel to the transition frequency line [red line in Fig. 3(e)], behaving as the canalization SPP mode [77]. When the frequency increases above the transition frequency, the topological transition from elliptic to hyperbolic takes place. Since the hyperbolic curve is open, the PTC resonance branches and the plasmon dispersion along the y axis would disappear. Thus, as shown in Fig. 3(e), when the frequency increases above the transition frequency, there are no resonance branches and plasmon dispersion along the y axis in the PTC in the (ω, k_y) plane.

We plot the heat-transfer coefficient h as a function of the vacuum gap in Fig. 4(a). To visualize the near-field enhancement effect for this material, Fig. 4(a) also shows the HTC of blackbody at room temperature given by $h_{\mathrm{bb}} = 4\sigma_{\mathrm{SB}} T^3 = 6.12$ W m^{-2} K^{-1}, where σ_{SB} is the Stefan-Boltzmann constant. It can be found that the heat-transfer rate of the monolayer T_d–WTe_2 system is colossally enhanced in the near-field region due to the evanescent contribution, which is several orders of magnitude higher than the blackbody limit. In particular, the results show that HTC for $d = 10$ nm is close to 7394 times enhancement over the blackbody limit (45.28 kW m^{-2} K^{-1}), even surpassing that of optimized black phosphorus sheets (6284 Q_{bb} at $T = 300$ K and $d = 10$ nm) by about 17.6% [50,78].

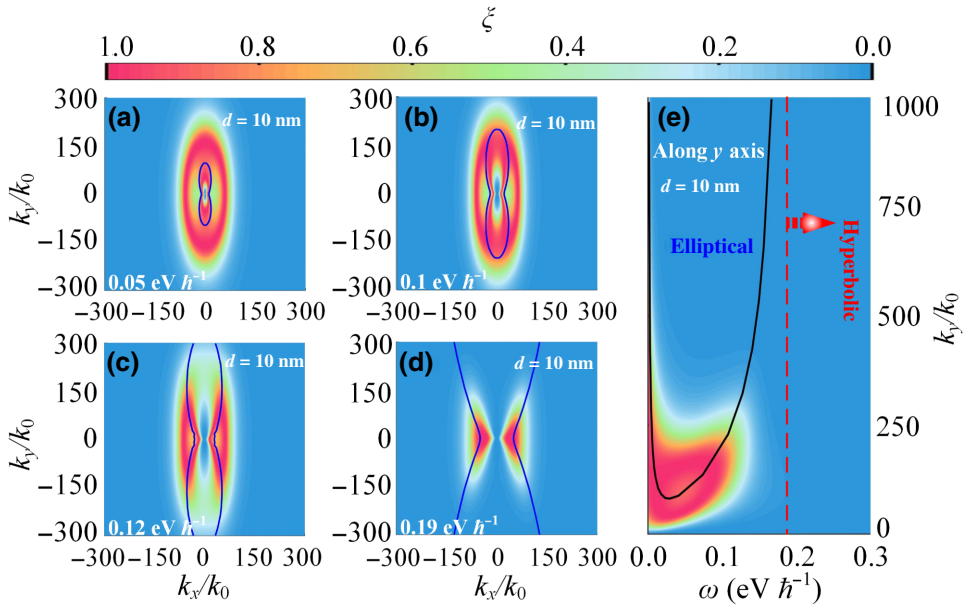

FIG. 3. PTC at frequencies of (a) 0.05, (b) 0.1, (c) 0.12, and (d) 0.19 eV/$\hbar$, and (e) along the y axis. The gap is $d = 10$ nm. The blue or black lines denote the dispersion of the T_d–WTe_2 plasmon at the frequencies given in each panel. The red line denotes the transition frequency.

According to the approximate expression in Ref. [79], the NFTR for any 2D materials tends to follow the unique asymptotic law of d^{-1} in the deep near field (approximately 10 nm). As shown in Fig. 4(a), when the gap is 10 nm, the HTC of T_d–WTe_2 approaches a d^{-1} dependence [plotted by the blue curve], following the approximate law of 2D materials proposed by Pablo *et al.* [79]. As the two T_d–WTe_2 sheets stay away from each other, this asymptotic law of d^{-1} gradually fails [79,80]. Due to exponential attenuation of available high local density of states, the NFTR of monolayer T_d–WTe_2 decreases rapidly and the attenuation tendency gradually transitions from d^{-1} to d^{-3} [79,80], as shown in Fig. 4(a). We further observe in Fig. 4(a) that there is a vacuum gap (approximately 1000 nm) at which the enhanced effect of heat transfer is converted to a suppression effect. That is, as the vacuum gap increases beyond the transition point, the radiative heat-transfer rate of the blackbody begins to outperform that of the monolayer T_d–WTe_2 system. In this case, since the large gap reduces the evanescent contribution of thermal radiation to negligible levels, propagating (i.e., nonevanescent) waves gradually play a predominant role. Besides, owing to the atomic thickness, this material tends to be optically transparent for propagating waves, resulting in a small radiative heat-transfer rate. As a result, while the vacuum gap is fixed at 10 μm, the monolayer T_d–WTe_2 system yields only a weak HTC of 0.0051 H_{bb}, as shown in Fig. 4(a). The spectral HTC contours for different vacuum gaps are presented in Fig. 4(b). One can see the spectral HTC for $d = 10$ nm peaks at 0.29 nW m^{-2} rad^{-1} s K^{-1}. As sketched in Fig. 4(b), the spectral peak decreases monotonically with the increase of gap due to the rapid decrease in the local density of states. While the vacuum gap increases to 90 nm, the maximum spectral HTC decreases rapidly to 0.015 nW m^{-2} rad^{-1} s K^{-1}, which explains to a great extent why the HTC is bigger at a smaller gap. Furthermore, Fig. 4(b) shows that the frequency corresponding to the spectral peak at a small vacuum gap (10 nm) is close to 0.103 eV/$\hbar$, while the spectral peak frequency is redshifted to around 0.06 eV for $d = 90$ nm. The notable frequency shift can be physically understood through the radiative attenuation depth. Since the radiative attenuation depth of the evanescent wave in vacuum is proportional to $1/(2\ \mathrm{Im}\{k_{z0}\})$, the evanescent wave with higher frequency attenuates more and is easily filtered out by the larger gap. Therefore, with the increasing of vacuum gap, the surface states at lower frequency gradually dominate the NFTR in Fig. 4(b). Although the wave-vector range of PTC is compressed obviously after topological transition, it still exhibits bright resonance branches, which is not consistent with drastic decay in the spectral HTC as depicted in Fig. 4(b). It is because in addition to the surface state, the mean photon energy Θ also plays a role in the NFTR [76,81–84]. Due to the exponential decay of the mean photon energy at room temperature, the surface states with higher frequency are difficult to excite with a strong spectral HTC. Therefore, in Fig. 4(b), when the frequency increases to the hyperbolic region, it is difficult to observe the enhancement of the spectral heat transfer excited by the HSPPs.

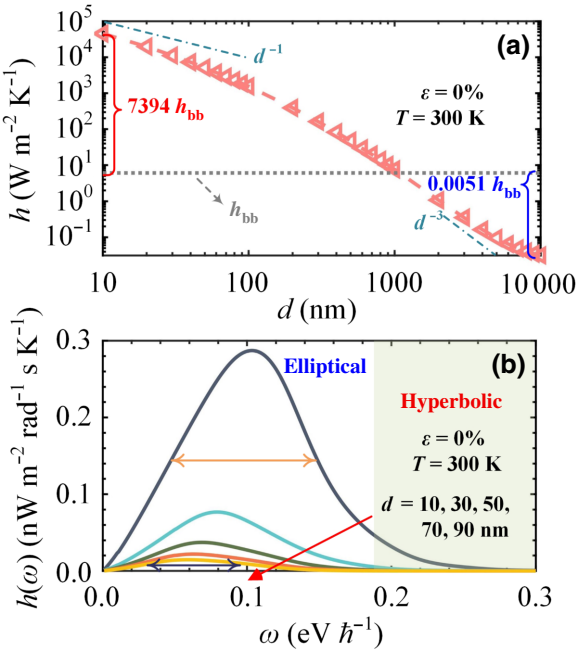

FIG. 4. (a) Heat-transfer coefficient h of a monolayer T_d–WTe_2 system as a function of the vacuum gap. (b) Spectral HTC $h(\omega)$ as a function of frequency for several vacuum gaps. The gray dotted line in (a) is the HTC for the blackbody. The hyperbolic regime in (b) is represented by the shaded area. The horizontal arrow in (b) denotes the bandwidth defined by the full width at half maximum.

IV. TUNABLE EFFECT OF MECHANICAL STRESS ON NEAR-FIELD RADIATIVE THERMAL RADIATION

It is worth mentioning that mechanical stress can strongly perturb the band structure, resulting in a notable modification of its electronic and photonic performances [41,42]. In particular, when a uniaxial tensile stress is applied to the W chains of T_d–WTe_2, the Weyl cone of this material transforms from the tilted to the normal, that is, this material undergoes a phase transition from type-II to type-I semimetal. The interband threshold energy and the Fermi surface also can be tuned considerably by the tensile stress [41,42], giving rise to the possibility of remarkable modifications of the optical response in T_d–WTe_2. In addition to the tensile stress, compressive stress can also play a role in modifying the optical response. In what follows, the dependences of the surface state and NFTR on the mechanical stress along the W chains, i.e., along the x direction are studied extensively. Besides, the modulation effects of mechanical stress along the y direction are provided in the Supplemental Material [60]. The stress along the y direction does not induce an obvious topological changes of the SPP and PTC, and therefore the main mechanism responsible for the increased NFTR in the case of tension along the y axis is the increase in the wave-vector range of the elliptic SPPs. As it is the case, for instance, in black phosphorous [50]. Figure 5 shows the imaginary part of the optical conductivity along two principal axes under stress $\varepsilon \in [-4\%, +4\%]$. Here, $+$ and $-$ represent the tensile and compressive stress. The value of the mechanical stress is defined as a relative change of the crystal unit-cell size along the direction of the strain as compared to the original cell size. For instance, a strain along the x direction is defined as $\varepsilon = (a - a_0)/a_0$, where a is the strained and a_0 is the original unit-cell sizes along the x direction. In the case of tensile stress, we find that with an increase in mechanical stress, the spectral windows of the hyperbolic regime (green) go down to a lower frequency and occupy a broad spectral bandwidth. For example, for $\varepsilon = 1\%$, the hyperbolic window of this material appears at 0.153 eV/$\hbar$, as shown in Fig. 5(a). When T_d–WTe_2 stands the tensile deformation with 3%, it is evident that the optical response of this material is hyperbolic over a broad frequency region from 0.081–0.3 eV/$\hbar$, as shown in Fig. 5(c). However, Fig. 5(d) shows that as the tensile stress further increases to 4%, the transition point has a slight blueshift. In contrast, for compressive stress, the hyperbolic window is blueshifted, as shown in Figs. 5(e)–5(h). When the compressive stress is fixed at -3%, it is difficult to observe the hyperbolic characteristic of this material in Fig. 5(g). Furthermore, the value of $\mathrm{Im}(\sigma_{xx,yy})$ is directly related to mechanical stress, and increases (decreases) with the increasing of compressive (tensile) stress, as depicted in Fig. 5.

To explore the microscopic mechanism of stress-induced effect further, we now turn to discussion of interband transitions and intraband transitions in T_d–WTe_2 at different stress (Fig. 6). Figure 6(a) exhibits the $\mathrm{Re}(\sigma)$ for x and y directions, revealing how both intraband Drude conductivities and interband excitations are anisotropic with respect to directions without mechanical stress. It can be seen that Drude response is larger at the x axis at around 1 eV, or $\mathrm{Re}(\sigma)$ is higher, implying interband excitations along Γ-Y direction between the highest occupied and the lowest unoccoupied bands are allowed as shown in Fig. 6(b). On the other hand, Fig. 6(a) shows $\mathrm{Re}(\sigma)$ for the y axis is smaller and interband transitions along Γ-Y are forbidden. However, since its interband threshold energy (frequency) ω_{ib} is too high, this surface state with higher frequency is difficult to excite with a strong NFTR. When the strain is applied, the interband threshold energy (frequency) along the Γ-Y direction is modified, as shown in Fig. 6(c). In the case of compressive stress, we find that with an increase in mechanical stress, interband threshold energy (frequency) goes down to a lower value, implying interband transitions gradually assume a more useful role in the NFTR with increased compressive stress. Meanwhile, in Fig. 6(c), we introduce the ratio between the dc conductivities along x and y axes, representing the measure of anisotropy of the intraband (Drude) channel. From these results it turns out that the modifications of the hyperbolic

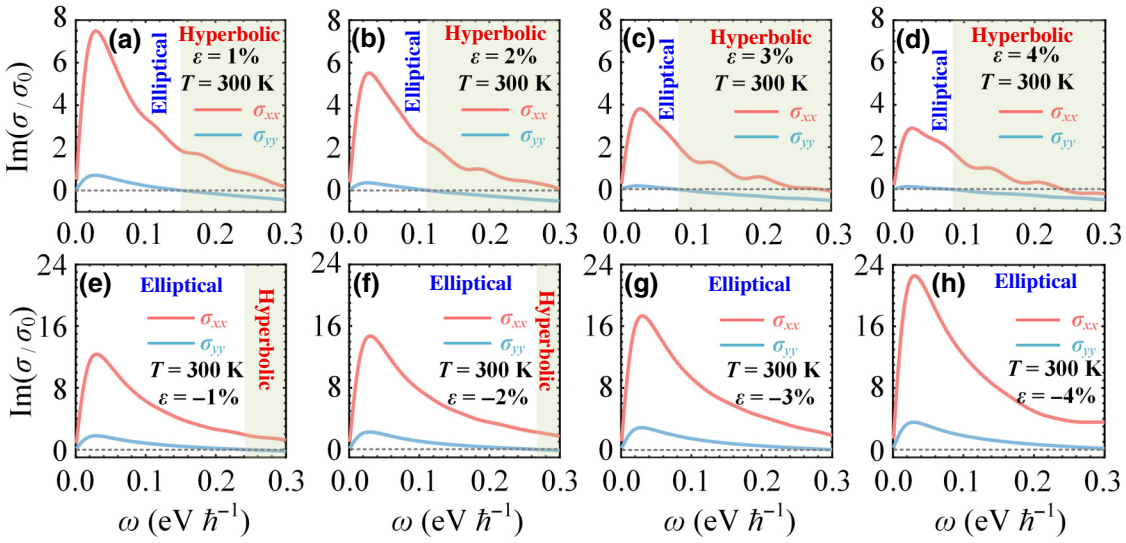

FIG. 5. Imaginary parts of the optical conductivity along the x axis (red) and the y axis (blue) at different mechanical stress (a)–(d) $\varepsilon = 1\%$, 2%, 3%, and 4% (tensile stress) or (e)–(h) $\varepsilon = -1\%$, -2%, -3%, and -4% (compressive stress). The hyperbolic regimes are depicted by shaded areas.

regions as well as the ensuing elliptical and hyperbolic near-field heat transport are induced by the interplay of these highly tunable anisotropy of intraband and interband excitations. Thus, according to the interband threshold energy and the ratio $\sigma_{\mathrm{dc},xx}/\sigma_{\mathrm{dc},yy}$ in Fig. 6(c), the above-mentioned interplay can be clearly exhibited. This renders the microscopic nature of the hyperbolic plasmons and the corresponding elliptic and hyperbolic NFTR in T_d–WTe_2 quite peculiar and unique.

Figure 7 shows HTC as a function of mechanical stress ε with a vacuum gap of 10 nm and a temperature of 300 K. In all cases, the HTCs between two T_d–WTe_2 sheets exceed the blackbody limit. In the case of tensile stress, we find that the HTC exhibits a nonmonotonic dependency versus the tensile stress, with the maximum HTC of 56.31 kW m^{-2} K^{-1} at $\varepsilon = 2\%$. With an additional increase in ε, Fig. 7 shows that although there is a downward trend, HTC remains at a relatively high level. For example, when the tensile stress increases to 4%, HTC can reach 1.1 times greater than that at $\varepsilon = 0\%$. In other words, the mechanical tensile stress provides us an active way to further enhance the NFTR. Note that a significant difference in NFTR is witnessed between the cases of compressive stress and tensile stress as depicted in Fig. 7. One can further see that, a monotonic decreasing of HTC is observed unambiguously with the increase of compressive stress. When T_d–WTe_2 is subjected to compressive deformation, the HTC decreases rapidly from 45.28 kW m^{-2} K^{-1} for $\varepsilon = 0\%$ to 34.04 kW m^{-2} K^{-1} for $\varepsilon = -1\%$. Figure 7 shows that T_d–WTe_2 only has a HTC of 15.62 kW m^{-2} K^{-1} for $\varepsilon = -4\%$.

In the plot of spectral HTCs of T_d–WTe_2 for different tensile deformations [Fig. 8(a)], we observe that the spectral HTCs exhibit notable changes. Figure 8(a) shows that the bandwidth of the spectral HTC is slightly modified as the tensile stress changes, whereas the maximum of the spectral HTC first increases and then descends, which is in agreement with the nonmonotonic trend of the HTC in Fig. 7. Here, the horizontal arrow denotes the bandwidth (full width at half maximum). For a small mechanical deformation ($\varepsilon \leq 2\%$), the ascending trend of the spectral peak is significant. The spectral peak can reach a high value of 0.29 nW m^{-2} rad^{-1} s K^{-1} for $\varepsilon = 0\%$ and increases rapidly to 0.39 nW m^{-2} rad^{-1} s K^{-1} for $\varepsilon = 2\%$. This result coincides with the sharp increase in the NFTR, as shown in Fig. 7. When the mechanical deformation exceeds 2%, the dependence of the spectral peak on tensile stress is weakened. For example, as we stretch T_d–WTe_2 from $\varepsilon = 3\%$ to $\varepsilon = 4\%$, the spectral peak decreases only from 0.38 to 0.35 nW m^{-2} rad^{-1} s K^{-1}. Furthermore, as shown in Fig. 8(a), with increased mechanical stress, due to the fact that the spectral window of the hyperbolic region decreases to a lower frequency, the spectral HTC induced by HSPPs occupies a broad bandwidth, indicating that HSPPs gradually play a more useful role in the NFTR of T_d–WTe_2. To present an intuitive insight of the influences of HSPPs and ESPPs on NFTR, in Fig. 8(b), we elaborate a little more on the energy distributions of HSPPs and ESPPs in radiative heat transfer under different tensile deformations. In terms of the hyperbolic surface mode, it can be shown that the NFTR resulting from this mode is very small [about 4%; see Fig. 8(b)] in the equilibrium case. As the tensile stress is applied, Fig. 8(b) shows that the contribution of the hyperbolic mode to radiative heat transfer is substantially enhanced. For instance, at room temperature, the proportion of heat flux supported by hyperbolic mode in the NFTR is increased from 4.03% to

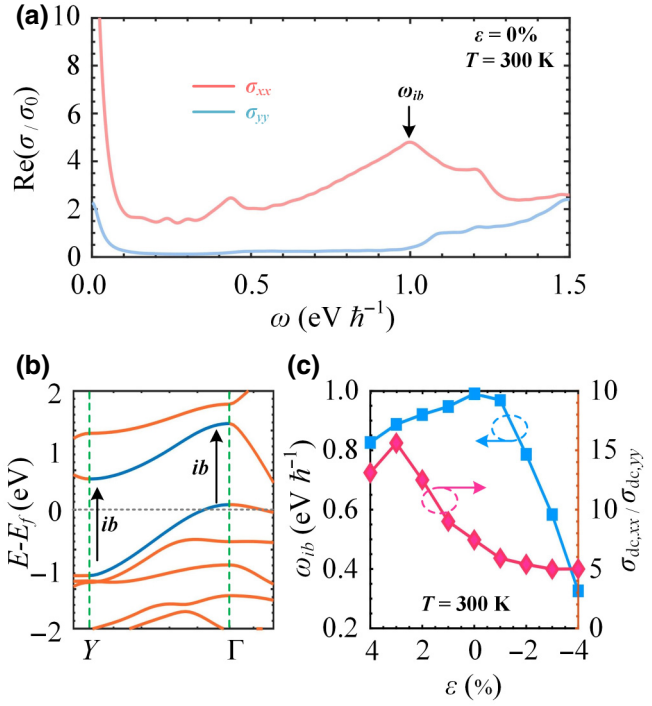

FIG. 6. (a) Real parts of the optical conductivity along the x axis (red) and the y axis (blue) without mechanical stress. (b) Electronic band structures for the monolayer T_d–WTe_2 along the high-symmetry points Y–Γ in the orthorhombic unit cell without mechanical stress. (c) The interband threshold energy (frequency) (left y axis) and the radio between dc conductivity along x and y axes (right y axis) at different mechanical stress.

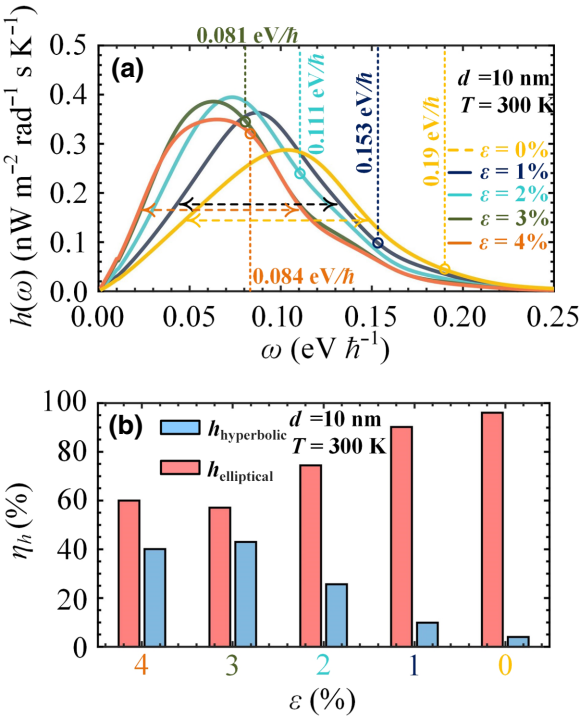

FIG. 8. (a) Spectral HTC as a function of frequency for several tensile stresses. The horizontal arrow in (a) denotes the bandwidth (full width at half maximum). The round marks represent elliptical-hyperbolic transition frequencies at several tensile stresses. (b) Energy distributions of HSPPs and ESPPs in NFTR under different mechanical deformations. The gap is $d = 10$ nm.

25.59%, by changing stress from $\varepsilon = 0\%$ to 2%. When the ε is fixed at 3%, the maximum proportion of 43.01% can be achieved in Fig. 8(b). Consequently, it can be concluded that the HSPPs together with ESPPs provide the dominant heat-flux channel when a large tensile stress is applied to the T_d–WTe_2.

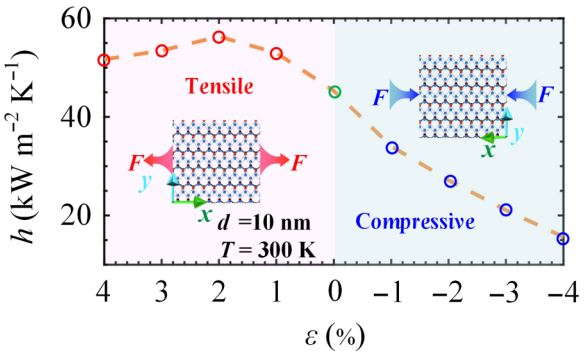

FIG. 7. HTC at a room temperature of 300 K for the T_d–WTe_2 system with different mechanical stress. The gap is $d = 10$ nm. The red and blue areas correspond to the tensile stress and the compressive stress, respectively.

Next, to better understand the mechanism behind the above results, in Fig. 9, we elaborate on the evolution of surface state under different tensile stresses. In particular, we illustrate the $\xi(\omega, k_x, k_y)$ with a tensile stress of 1%, 2%, 3%, and 4%, respectively, in Figs. 9(a)–9(d). The top row shows the PTCs with different tensile stresses at the frequency of 0.05 eV/$\hbar$. Notice first that at the frequency of 0.05 eV/$\hbar$ the bright branches of the T_d–WTe_2 under all tensile stresses remain elliptical, matching very well with the result and analysis mentioned above. The top row of Fig. 9 shows that with the increase of tensile stress, the electromagnetic mode along the y axis occupies a broader wave-vector region, while its surface state diminishes. However, a similar plot does not occur for the electromagnetic mode along the x axis. It is clear from these results that as the tensile stress increases, the surface states along the x axis produce a stronger bright branch, which means that the NFTR of T_d–WTe_2 with heavy-tensile deformation is dominated by the surface states along the W-chain direction (x axis) at low frequency. To confirm the low-frequency evolution of these surface states for different tensile stresses, we also plot the plasmon dispersion relations in the top row of Fig. 9 denoted by the blue curves. It can be seen that the blue curves are unambiguously located

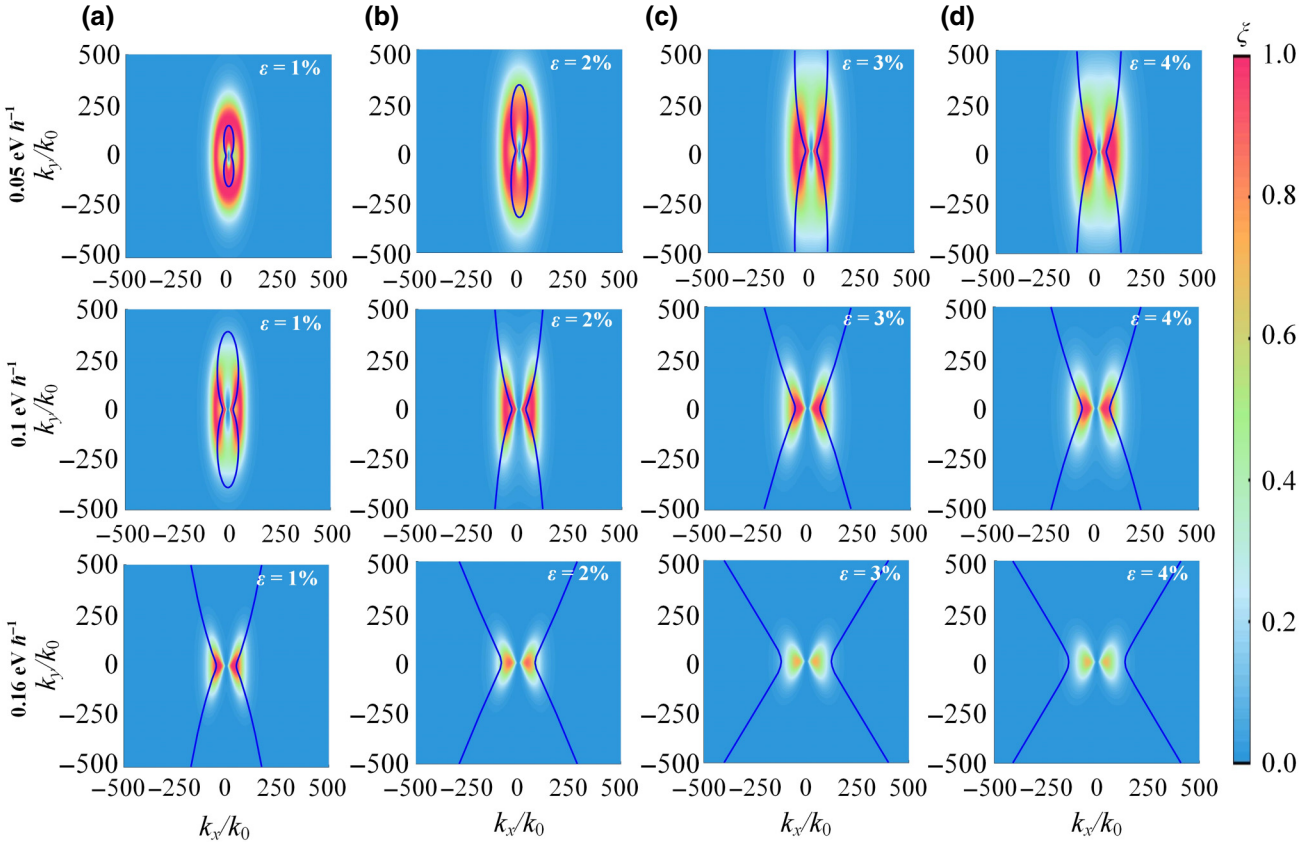

FIG. 9. PTCs at frequencies of 0.05 eV/$\hbar$ (top row), 0.1 eV/$\hbar$ (middle row), and 0.16 eV/$\hbar$ (bottom row) with tensile stresses of (a) $\varepsilon = 1\%$, (b) $\varepsilon = 2\%$, (c) $\varepsilon = 3\%$, and (d) $\varepsilon = 4\%$. The blue curves correspond to the plasmon dispersions of the T_d–WTe_2. The gap size is $d = 10$ nm.

in the bright branches, confirming that the ESPPs indeed play a dominant role in the NFTR of T_d–WTe_2 for all tensile stresses at this frequency. Moreover, the top row of Fig. 9 shows that the increase in the tensile stress expands the elliptic dispersion curve to a higher wave-vector range. In particular, when we apply a 3% tensile stress to this material, the plasmon dispersion relations along the y axis extend to a region above 500 k_0. This phenomenon is explained by the decline in T_d–WTe_2 conductivity, that is, Im (σ_{yy}) decreases from 0.58 σ_0 at $\varepsilon = 1\%$ to 0.09 σ_0 at $\varepsilon = 3\%$, which is shown in Fig. 5. However, it can be seen that the bright branches do not extend significantly into the larger wave-vector region (>500 k_0) for $\varepsilon = 3\%$ and $\varepsilon = 4\%$ with the dispersion curve in the top row of Fig. 9. This is because the attenuation length of the surface mode in the high wave-vector region decreases sharply. At the higher wave-vector region, the evanescent wave is easily filtered by the vacuum gap [76], which no longer stimulates the obvious coupling effect of SPPs between two monolayer T_d–WTe_2 sheets.

The middle row of Fig. 9 draws the PTCs with different tensile stresses corresponding to the frequency of 0.1 eV/$\hbar$. As mechanical deformation reaches 2%, the near-zero conductivity along the y axis [$\mathrm{Im}(\sigma_{yy}) = 0.04\ \sigma_0$] leads to a great extension of the dispersion in this material. In this scenario, it is difficult to observe the distinct coupled resonance branch along the y axis due to the strong attenuation of the evanescent wave in the large wave-vector region, therefore resulting in the bright branches like hyperbolas. However, it is worth noting that in this scenario the NFTR of this material is still dominated by ESPPs due to $\mathrm{Im}(\sigma_{yy}) \times \mathrm{Im}(\sigma_{xx}) > 0$. As the tensile stress further increases, the in-plane surface state evolves from an ellipse to a hyperbola, that is, $\mathrm{Im}(\sigma_{yy}) \times \mathrm{Im}(\sigma_{xx}) < 0$. We find that the dispersion topologically transforms into hyperbola, in agreement with the PTC contour, as shown in the middle row of Fig. 9(c). Since the hyperbolic curve is open, ideally, there is no limit to the density of states [34]. Practically, because of the intrinsic decay of the photon tunneling in the high wave vector, the evanescent contribution is weak when the wave vector goes to high k. When the frequency is increased to 0.16 eV/$\hbar$, the surface modes of the T_d–WTe_2 for all tensile stresses enter the hyperbolic window, as shown in the optical conductivity of Fig. 5.

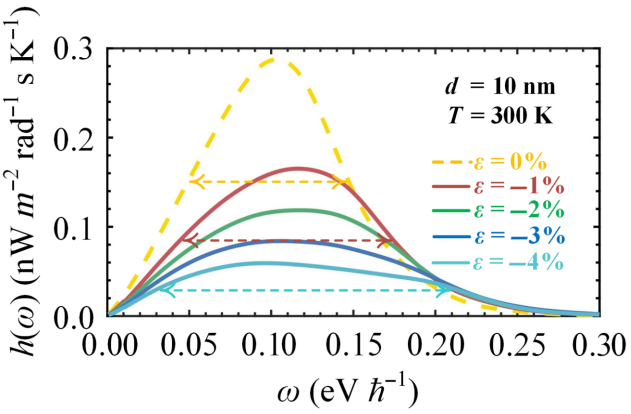

FIG. 10. Spectral HTC as a function of frequency for several compressive stresses. The horizontal arrow denotes the bandwidth (full width at half maximum). The gap is $d = 10$ nm.

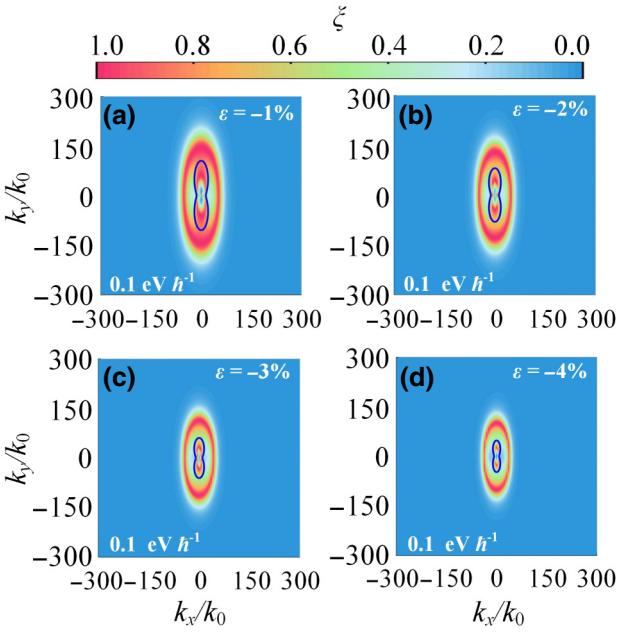

FIG. 11. PTC at a frequency of 0.1 eV/$\hbar$ with a compressive stress of (a) $\varepsilon = -1\%$, (b) $\varepsilon = -2\%$, (c) $\varepsilon = -3\%$, and (d) $\varepsilon = -4\%$. The blue curves correspond to the plasmon dispersions of the T_d–WTe_2. The gap size is $d = 10$ nm.

These can be seen more clearly by drawing the PTC contours and dispersion curves in the bottom row of Fig. 9. As the deformation increases from 1% to 3%, the wave vector of HSPPs is significantly compressed to a lower region, which suppresses the spectral HTC at this frequency. When the tensile stress exceeds 3%, we observe that in the bottom row of Figs. 9(c) and 9(d), the PTC contours and dispersion curves of two deformations nearly coincide with each other. In other words, under the heavy deformation ($\varepsilon \geq 3\%$), the modification effect of the tensile stress on the hyperbolic surface state of T_d–WTe_2 reaches saturation. A similar trend can be observed in the lower frequency region [the middle row of Figs. 9(c) and 9(d)]. This phenomenon also explains well why the spectral HTCs of $\varepsilon = 3\%$ and $\varepsilon = 4\%$ nearly coincide with each other in the hyperbolic region, which is shown in Fig. 8(a).

Now we discuss the spectral results with different compressive deformations. Figure 10 shows that with the increasing of compressive deformation, although the spectral HTC occupies a broader spectral bandwidth, the spectral peak significantly decreases, thereby weakening the NFTR. For instance, the spectral peak can obtain a high value of 0.16 nW m^{-2} rad^{-1} s K^{-1} for $\varepsilon = -1\%$ and decreases rapidly to 0.06 nW m^{-2} rad^{-1} s K^{-1} for $\varepsilon = -4\%$. This result coincides with the sharp decline in the NFTR, as shown in Fig. 7. Next, in order to better understand the mechanism behind the above results, we analyze in Fig. 11 the PTC and the plasmon dispersion under different compressive deformations. We show in Figs. 11(a)–11(d) $\xi(\omega, k_x, k_y)$ for compressive deformations of −1%, −2%, −3%, and −4%, respectively. The frequency is taken as 0.1 eV/$\hbar$. Notice first that the bright branches of the T_d–WTe_2 sheet under all compressive stresses remain elliptical in Fig. 11; that is, the compressive stress does not transform the topology of this material at this frequency. With the increase of compressive deformation, the PTC in all directions can hold a robust bright branch, but its wave vector is significantly compressed to a smaller region. As can be seen from Figs. 11(a) and 11(d), the wave-vector range along the y axis decreases from $\{-223, 223\}k_0$ to $\{-150, 150\}k_0$ as ε increases from −1% to −4%. Therefore, according to the above results, the main mechanism responsible for the reduced NFTR in the case of compression is the reduction in the wave-vector range of elliptic SPPs. This feature is more manifest in the plasmon dispersion of the SPPs given in Fig. 11 where the plasmon dispersion in k space for different compressive deformations is also plotted. Figure 11(a) shows that, for the compressive deformation of −1%, the maximum plasmon dispersion along the y axis extends to 105 k_0. With the increasing of ε, the dispersion lines along all directions move toward a lower wave vector. When the compressive deformation is taken as −4%, the maximum plasmon dispersion along the y axis shrinks drastically to 48 k_0, greatly limiting the wave-vector region of SPPs.

V. CONCLUSION

In conclusion, we investigate radiative heat transport between two monolayer T_d–WTe_2 by combining density-functional theory and fluctuation-dissipation theory. We demonstrate that monolayer T_d–WTe_2 is a natural two-dimensional plasmonic material with a strong surface state, supporting 3-order-of-magnitude enhancement of thermal

radiation over the blackbody limit. By analyzing the photonic tunneling coefficient as well as the plasmon dispersion relation of T_d–WTe_2, the elliptical and hyperbolic plasmonic properties of this 2D material are exhibited, and the contributions from different plasmonic modes to the radiative heat transfer in T_d–WTe_2 are revealed. Furthermore, the calculations demonstrate that the optical response in T_d–WTe_2 can be tuned effectively by modifying the unique anisotropy of the Fermi surface and the interband excitation threshold under mechanical deformation, triggering a topological transition between the elliptic and hyperbolic regimes. We systematically examine the effects of compressive and tensile stress on the plasmonic properties in T_d–WTe_2. After that, we investigate the modulation of compressive and tensile stress on NFTR. It is found that a significant enhancement (125%) of heat flux can be achieved by applying an appropriate tensile stress, which has never been noted in the noncontact heat exchanges at the nanoscale.

This work not only shines light on the near-field radiative peculiarity of natural two-dimensional hyperbolic materials, but also reveals the possibility to apply mechanical deformation for active thermal management of this material at the nanoscale. Moreover, it is hoped that the reported tunable hyperbolic plasmons of this material would provide some guidance for optoelectronic devices.

ACKNOWLEDGMENTS

This work is supported by the National Natural Science Foundation of China (Grant No. 52076056), the Fundamental Research Funds for the Central Universities (Grant No. FRFCU5710094020), the Shandong Provincial Natural Science Foundation (Grant No. ZR2020LLZ004), the National Natural Science Foundation of China (Grant No. 52106099), the Croatian Science Foundation (Grant no. UIP-2019-04-6869), and the European Regional Development Fund for the "Center of Excellence for Advanced Materials and Sensing Devices" (Grant No. KK.01.1.1.01.0001)

[1] D. Polder and M. Van Hove, Theory of radiative heat transfer between closely spaced bodies, Phys. Rev. B **4**, 3303 (1971).

[2] S. Shen, A. Narayanaswamy, and G. Chen, Surface phonon polaritons mediated energy transfer between nanoscale gaps, Nano. Lett. **9**, 2909 (2009).

[3] Z. M. Zhang, *Nano/Microscale Heat Transfer* (Springer Nature, Switzerland, AG, 2020).

[4] S.-A. Biehs, R. Messina, P. S. Venkataram, A. W. Rodriguez, J. C. Cuevas, and P. Ben-Abdallah, Near-field radiative heat transfer in many-body systems, Rev. Mod. Phys. **93**, 025009 (2021).

[5] J. DeSutter, L. Tang, and M. Francoeur, A near-field radiative heat transfer device, Nat. Nanotechnol. **14**, 751 (2019).

[6] K. Kim, B. Song, V. Fernandez-Hurtado, W. Lee, W. H. Jeong, L. J. Cui, D. Thompson, J. Feist, M. T. H. Reid, F. J. Garcia-Vidal, J. C. Cuevas, E. Meyhofer, and P. Reddy, Radiative heat transfer in the extreme near field, Nature **528**, 387 (2015).

[7] R. St-Gelais, B. Guha, L. X. Zhu, S. H. Fan, and M. Lipson, Demonstration of strong near-field radiative heat transfer between integrated nanostructures, Nano. Lett. **14**, 6971 (2014).

[8] J. Yang, W. Du, Y. S. Su, Y. Fu, S. X. Gong, S. L. He, and Y. G. Ma, Observing of the super-planckian near-field thermal radiation between graphene sheets, Nat. Commun. **9**, 4033 (2018).

[9] M. Ghashami, H. Y. Geng, T. Kim, N. Iacopino, S. K. Cho, and K. Park, Precision Measurement of Phonon-Polaritonic Near-Field Energy Transfer Between Macroscale Planar Structures Under Large Thermal Gradients, Phys. Rev. Lett. **120**, 175901 (2018).

[10] M. Lim, J. Song, S. S. Lee, and B. J. Lee, Tailoring near-field thermal radiation between metallo-dielectric multilayers using coupled surface plasmon polaritons, Nat. Commun. **9**, 4302 (2018).

[11] X. R. Zheng, A. Calo, E. Albisetti, X. Y. Liu, A. S. M. Alharbi, G. Arefe, X. C. Liu, M. Spieser, W. J. Yoo, T. Taniguchi, K. Watanabe, C. Aruta, A. Ciarrocchi, A. Kis, B. S. Lee, M. Lipson, J. Hone, D. Shahrjerdi, and E. Riedo, Patterning metal contacts on monolayer MoS_2 with vanishing Schottky barriers using thermal nanolithography, Nat. Electron. **2**, 17 (2019).

[12] B. Zhao, S. Assawaworrarit, P. Santhanam, M. Orenstein, and S. H. Fan, High-performance photonic transformers for DC voltage conversion, Nat. Commun. **12**, 4684 (2021).

[13] C. Guo, B. Zhao, D. H. Huang, and S. H. Fan, Radiative thermal router based on tunable magnetic Weyl semimetals, ACS Photonics **7**, 3257 (2020).

[14] P. Ben-Abdallah, Photon Thermal Hall Effect, Phys. Rev. Lett. **116**, 084301 (2016).

[15] C. R. Otey, W. T. Lau, and S. H. Fan, Thermal Rectification Through Vacuum, Phys. Rev. Lett. **104**, 154301 (2010).

[16] A. Fiorino, D. Thompson, L. X. Zhu, R. Mittapally, S. A. Biehs, O. Bezencenet, N. El-Bondry, S. Bansropun, P. Ben-Abdallah, E. Meyhofer, and P. Reddy, A thermal diode based on nanoscale thermal radiation, ACS Nano **12**, 5774 (2018).

[17] V. Kubytskyi, S.-A. Biehs, and P. Ben-Abdallah, Radiative Bistability and Thermal Memory, Phys. Rev. Lett. **113**, 074301 (2014).

[18] S.-A. Biehs and P. Ben-Abdallah, Near-Field Thermal Transistor, Phys. Rev. Lett. **112**, 044301 (2014).

[19] N. H. Thomas, M. C. Sherrott, J. Broulliet, H. A. Atwater, and A. J. Minnich, Electronic modulation of near-field radiative transfer in graphene field effect heterostructures, Nano Lett. **19**, 3898 (2019).

[20] J. Ordonez-Miranda, Y. Ezzahri, J. A. Tiburcio-Moreno, K. Joulain, and J. Drevillon, Radiative Thermal Memristor, Phys. Rev. Lett. **123**, 025901 (2019).

[21] A. Narayanaswamy and G. Chen, Surface modes for near field thermophotovoltaics, Appl. Phys. Lett. **82**, 3544 (2003).

[22] C. Lucchesi, D. Cakiroglu, J. P. Perez, T. Taliercio, E. Tournie, P. O. Chapuis, and R. Vaillon, Near-field

thermophotovoltaic conversion with high electrical power density and cell efficiency above 14%, Nano Lett. **21**, 4524 (2021).
[23] A. Fiorino, L. X. Zhu, D. Thompson, R. Mittapally, P. Reddy, and E. Meyhofer, Nanogap near-field thermophotovoltaics, Nat. Nanotechnol. **13**, 806 (2018).
[24] X. L. Liu and Z. M. Zhang, High-performance electroluminescent refrigeration enabled by photon tunneling, Nano Energy. **26**, 353 (2016).
[25] K. F. Chen, P. Santhanam, and S. H. Fan, Near-Field Enhanced Negative Luminescent Refrigeration, Phys. Rev. Appl. **6**, 024014 (2016).
[26] L. X. Zhu, A. Fiorino, D. Thompson, R. Mittapally, E. Meyhofer, and P. Reddy, Near-field photonic cooling through control of the chemical potential of photons, Nature **566**, 239 (2019).
[27] S.-A. Biehs, P. Ben-Abdallah, F. S. S. Rosa, K. Joulain, and J. J. Greffet, Nanoscale heat flux between nanoporous materials, Opt. Express **19**, A1088 (2011).
[28] S.-A. Biehs, M. Tschikin, and P. Ben-Abdallah, Hyperbolic Metamaterials as an Analog of a Blackbody in the Near Field, Phys. Rev. Lett. **109**, 104301 (2012).
[29] S. Basu and L. P. Wang, Near-field radiative heat transfer between doped silicon nanowire arrays, Appl. Phys. Lett. **102**, 053101 (2013).
[30] J. L. Song and Q. Cheng, Near-field radiative heat transfer between graphene and anisotropic magneto-dielectric hyperbolic metamaterials, Phys. Rev. B **94**, 125419 (2016).
[31] S.-A. Biehs, M. Tschikin, R. Messina, and P. Ben-Abdallah, Super-Planckian near-field thermal emission with phonon-polaritonic hyperbolic metamaterials, Appl. Phys. Lett. **102**, 131106 (2013).
[32] X. L. Liu, T. J. Bright, and Z. M. Zhang, Application conditions of effective medium theory in near-field radiative heat transfer between multilayered metamaterials, J. Heat. Transfer-Trans. ASME **136**, 092703 (2014).
[33] E. Moncada-Villa and J. C. Cuevas, Near-field radiative heat transfer between one-dimensional magnetophotonic crystals, Phys. Rev. B **103**, 075432 (2021).
[34] X. L. Liu and Z. M. Zhang, Giant enhancement of nanoscale thermal radiation based on hyperbolic graphene plasmons, Appl. Phys. Lett. **107**, 143114 (2015).
[35] X. L. Liu and Z. M. Zhang, Near-field thermal radiation between metasurfaces, ACS Photonics **2**, 1320 (2015).
[36] V. Fernandez-Hurtado, F. J. Garcia-Vidal, S. H. Fan, and J. C. Cuevas, Enhancing Near-Field Radiative Heat Transfer with Si-Based Metasurfaces, Phys. Rev. Lett. **118**, 203901 (2017).
[37] O. D. Miller, S. G. Johnson, and A. W. Rodriguez, Effectiveness of Thin Films in Lieu of Hyperbolic Metamaterials in the Near Field, Phys. Rev. Lett. **112**, 157402 (2014).
[38] A. Nemilentsau, T. Low, and G. Hanson, Anisotropic 2D Materials for Tunable Hyperbolic Plasmonics, Phys. Rev. Lett. **116**, 066804 (2016).
[39] D. N. Basov, M. M. Fogler, and F. J. Garcia de Abajo, Polaritons in van der Waals materials, Science **354**, aag1992 (2016).
[40] H. W. Wang and T. Low, Hyperbolicity in two-dimensional transition metal ditellurides induced by electronic bands nesting, Phys. Rev. B **102**, 241104 (2020).
[41] Z. Torbatian, D. Novko, and R. Asgari, Tunable Low-Loss Hyperbolic Plasmon Polaritons in a T_d-WTe_2 Single Layer, Phys. Rev. Appl. **14**, 044014 (2020).
[42] E. van Veen, A. Nemilentsau, A. Kumar, R. Roldan, M. I. Katsnelson, T. Low, and S. J. Yuan, Tuning Two-Dimensional Hyperbolic Plasmons in Black Phosphorus, Phys. Rev. Appl. **12**, 014011 (2019).
[43] M. Dehdast, Z. Valiollahi, M. Neek-Amal, B. Van Duppen, F. M. Peeters, and M. Pourfath, Tunable natural terahertz and mid-infrared hyperbolic plasmons in carbon phosphide, Carbon **178**, 625 (2021).
[44] C. Wang, S. Y. Huang, Q. X. Xing, Y. G. Xie, C. Y. Song, F. J. Wang, and H. G. Yan, Van der waals thin films of WTe_2 for natural hyperbolic plasmonic surfaces, Nat. Commun. **11**, 1158 (2020).
[45] C. Wang, Y. Y. Sun, S. Y. Huang, Q. X. Xing, G. W. Zhang, C. Y. Song, F. J. Wang, Y. G. Xie, Y. C. Lei, Z. Z. Sun, and H. G. Yan, Tunable Plasmons in Large-Area WTe_2 Thin Films, Phys. Rev. Appl. **15**, 014010 (2021).
[46] T. Low, A. Chaves, J. D. Caldwell, A. Kumar, N. X. Fang, P. Avouris, T. F. Heinz, F. Guinea, L. Martin-Moreno, and F. Koppens, Polaritons in layered two-dimensional materials, Nat. Mater. **16**, 182 (2017).
[47] K. T. Lam and J. Guo, Plasmonics in strained monolayer black phosphorus, J. Appl. Phys. **117**, 113105 (2015).
[48] L. X. Ge, K. Gong, Y. P. Cang, Y. S. Luo, X. Shi, and Y. Wu, Magnetically tunable multiband near-field radiative heat transfer between two graphene sheets, Phys. Rev. B **12**, 035414 (2019).
[49] O. Ilic, M. Jablan, J. D. Joannopoulos, I. Celanovic, H. Buljan, and M. Soljačić, Near-field thermal radiation transfer controlled by plasmons in graphene, Phys. Rev. B **85**, 155422 (2012).
[50] Y. Zhang, H. L. Yi, and H. P. Tan, Near-field radiative heat transfer between black phosphorus sheets via anisotropic surface plasmon polaritons, ACS Photonics **5**, 3739 (2018).
[51] T. Zhu, Z. Q. Zhang, Z. B. Gao, and J. S. Wang, First-Principles Method to Study Near-Field Radiative Heat Transfer, Phys. Rev. Appl. **14**, 024080 (2020).
[52] O. D. Miller, O. Ilic, T. Christensen, M. T. H. Reid, H. A. Atwater, J. D. Joannopoulos, M. Soljačić, and S. G. Johnson, Limits to the optical response of graphene and two-dimensional materials, Nano Lett. **17**, 5408 (2017).
[53] F. W. Yang and B. Song, Near-field thermal transport between two identical twisted bilayer graphene sheets separated by a vacuum gap, Phys. Rev. B **103**, 235415 (2021).
[54] X. L. Liu, J. D. Shen, and Y. M. Xuan, Near-field thermal radiation of nanopatterned black phosphorene mediated by topological transitions of phosphorene plasmons, Nanoscale Microscale Thermophys. Eng. **23**, 188 (2019).
[55] O. Ilic, N. H. Thomas, T. Christensen, M. C. Sherrott, M. Soljačić, A. J. Minnich, O. D. Miller, and H. A. Atwater, Active radiative thermal switching with graphene plasmon resonators, Nano Lett. **12**, 2474 (2018).
[56] S.-A. Biehs, F. S. S. Rosa, and P. Ben-Abdallah, Modulation of near-field heat transfer between two gratings, Appl. Phys. Lett. **98**, 243102 (2011).
[57] G. M. Tang, J. Chen, and L. Zhang, Twist-induced control of near-field heat radiation between magnetic weyl semimetals, ACS Photonics **8**, 443 (2021).

[58] H. H. Wu, Y. Huang, L. J. Cui, and K. Y. Zhu, Active Magneto-Optical Control of Near-Field Radiative Heat Transfer Between Graphene Sheets, Phys. Rev. Appl. **11**, 054020 (2019).

[59] C. L. Zhou, S. H. Yang, Y. Zhang, and H. L. Yi, Near-field electromagnetic heat transfer through nonreciprocal hyperbolic graphene plasmons, Nanoscale Microscale Thermophys. Eng. **24**, 168 (2020).

[60] See Supplemental Material at http://link.aps.org/supplemental/10.1103/PhysRevApplied.17.014044 for (1) expression for transmission and reflection coefficients of the anisotropic 2D material; (2) plasmon dispersion formulation for anisotropic 2D material; (3) tunable effect of mechanical stress along the y axis on near-field radiative thermal radiation, which includes Refs. [61–68] [85–87].

[61] C. L. Zhou, X. H. Wu, Y. Zhang, and H. L. Yi, Super-Planckian thermal radiation in borophene sheets, Int. J. Heat Mass Transfer **183**, 122140 (2022).

[62] A. Lakhatakia, Green's functions and Brewster condition for a half space bounded by an anisotropic impedance plane, Int. J. Infrared Millimeter Waves **13**, 631 (1992).

[63] J. S. Gomez-Diaz, M. Tymchenko, and A. Alù, Hyperbolic metasurfaces: Surface plasmons, light-matter interactions, and physical implementation using graphene strips, Opt. Mater. Express **5**, 2313 (2015).

[64] H. J. Bilow, Guided waves on a planar tensor impedance surface, IEEE Trans. Antennas Propag. **51**, 2788 (2003).

[65] M. Nakayama, Theory of surface waves coupled to surface carriers, J. Phys. Soc. Jpn. **36**, 393 (1974).

[66] K. W. Chiu and J. J. Quinn, Plasma oscillations of a two-dimensional electron gas in a strong magnetic field, Phys. Rev. B **9**, 4724 (1974).

[67] O. V. Kotov and Y. E. Lozovik, Hyperbolic hybrid waves and optical topological transitions in few-layer anisotropic metasurfaces, Phys. Rev. B **100**, 165424 (2019).

[68] M. Q. Yuan, Y. Zhang, S. H. Yang, and H. L. Yi, Active control of the near-field radiative heat transfer between two metal plates through the external electric field, Int. J. Therm. Sci. **171**, 107208 (2022).

[69] S. Y. Xu, Q. Ma, H. T. Shen, V. Fatemi, S. F. Wu, T. R. Chang, G. Q. Chang, A. M. M. Valdivia, C. K. Chan, Q. D. Gibson, J. D. Zhou, Z. Liu, K. Watanabe, T. Taniguchi, H. Lin, R. J. Cava, L. Fu, N. Gedik, and P. Jarillo-Herrero, Electrically switchable Berry curvature dipole in the monolayer topological insulator WTe_2, Nat. Phys. **14**, 900 (2018).

[70] Q. S. Wang, J. C. Zheng, Y. He, J. Cao, X. Liu, M. Y. Wang, J. C. Ma, J. W. Lai, H. Lu, S. Jia, D. Y. Yan, Y. G. Shi, J. X. Duan, J. F. Han, W. D. Xiao, J. H. Chen, K. Sun, Y. G. Yao, and D. Sun, Robust edge photocurrent response on layered type II Weyl semimetal WTe_2, Nat. Commun. **10**, 5736 (2019).

[71] D. Novko, M. Sunjic, and V. Despoja, Optical absorption and conductivity in quasi-two-dimensional crystals from first principles: Application to graphene, Phys. Rev. B **93**, 125413 (2016).

[72] Z. Torbatian, M. Alidoosti, D. Novko, and R. Asgari, Low-loss two-dimensional plasmon modes in antimonene, Phys. Rev. B **101**, 205412 (2020).

[73] Z. Torbatian and R. Asgari, Optical absorption properties of few-layer phosphorene, Phys. Rev. B **98**, 205407 (2018).

[74] P. Giannozzi, S. Baroni, N. Bonini, M. Calandra, R. Car, C. Cavazzoni, D. Ceresoli, G.L. Chiarotti, M. Cococcioni, I. Dabo, *et al.*, QUANTUM ESPRESSO: a modular and open-source software project for quantum simulations of materials, J. Phys.: Condens. Matter **21**, 395502 (2009).

[75] M. Francoeur, Ph.D. dissertation, University of Kentucky, 2010.

[76] R. Messina, P. Ben-Abdallah, B. Guizal, and M. Antezza, Graphene-based amplification and tuning of near-field radiative heat transfer between dissimilar polar materials, Phys. Rev. B **96**, 045402 (2017).

[77] Q. Yan, R. Chen, Z. Yuan, P. Li, and X. L. Zhang, Canalization acoustic phonon polaritons in metal-MoO3-metal sandwiched structures for nano-light guiding and manipulation, J. Opt. **24**, 024006 (2021).

[78] J. D. Shen, S. Guo, X. L. Liu, B. Liu, W. T. Wu, and H. He, Super-Planckian thermal radiation enabled by coupled quasi-elliptic 2D black phosphorus plasmons, Appl. Therm. Eng. **144**, 403 (2018).

[79] R. L. Pablo, T. Wang-Kong, and A. R. D. Diego, Radiative heat transfer in 2D Dirac materials, J. Phys.: Condens. Matter **27**, 214019 (2015).

[80] J. H. Jiang and J. S. Wang, Caroli formalism in near-field heat transfer between parallel graphene sheets, Phys. Rev. B **96**, 155437 (2017).

[81] J. B. Peng, G. M. Tang, L. Q. Wang, R. Macedo, H. Chen, and J. Ren, Twist-induced near-field thermal switch using nonreciprocal surface magnon-polaritons, ACS Photonics **8**, 2183 (2021).

[82] Y. Liu, F. Q. Chen, A. Caratenuto, and Y. Zheng, Dynamic tuning of near-field radiative transport between an overlapping pair of movable comb-like metamaterials, Appl. Phys. Lett. **118**, 153106 (2021).

[83] K. Z. Shi, Y. C. Sun, Z. Y. Chen, N. He, F. L. Bao, J. Evans, and S. L. He, Colossal enhancement of near-field thermal radiation across hundreds of nanometers between millimeter-scale plates through surface plasmon and phonon polaritons coupling, Nano Lett. **19**, 8082 (2019).

[84] Y. H. Kan, C. Y. Zhao, and Z. M. Zhang, Near-field radiative heat transfer in three-body systems with periodic structures, Phys. Rev. B **99**, 035433 (2019).

[85] J. S. Gomez-Diaz, M. Tymchenko, and A. Alu, Hyperbolic Plasmons and Topological Transitions Over Uniaxial Metasurfaces, Phys. Rev. Lett. **114**, 233901 (2016).

[86] T. Zhan, X. Shi, Y. Y. Dai, X. H. Liu, and J. Zi, Transfer matrix method for optics in graphene layers, J. Phys.: Condens. Matter **25**, 215301 (2013).

[87] P. Yeh, Electromagnetic propagation in birefringent layered media, J. Opt. Soc. Am. **69**, 742 (1979).